The variation of Mn-dopant distribution state with x and its effect on the magnetic coupling mechanism in $Zn_{1-x}Mn_xO$ nanocrystals*

Cheng Yan(程 岩)[a], Hao Wei-Chang(郝维昌)[a)b)†], Li Wen-Xian(李文献)[b)c)], Xu Huai-Zhe(许怀哲)[a)‡], Chen Rui(陈 蕊)[d)], and Dou Shi-Xue(窦士学)[b)]

[a)] *Department of Physics and Center of Materials Physics and Chemistry, Beihang University, Beijing* 100191, *China*
[b)] *Institute for Superconducting and Electronic Materials (ISEM), University of Wollongong, Wollongong, NSW* 2522, *Australia*
[c)] *Solar Energy Technologies, School of Computing, Engineering and Mathematics, University of Western Sydney, Penrith, NSW* 2751, *Australia*
[d)] *State Key Laboratory of Inorganic Synthesis and Preparative Chemistry, College of Chemistry, Jilin University, Changchun* 130012, *China*

(Received 16 April 2013; revised manuscript received 9 May 2013)

$Zn_{1-x}Mn_xO$ ($x = 0.0005$, 0.001, 0.005, 0.01, 0.02) nanocrystals are synthesized by using a wet chemical process. The coordination environment of Mn is characterized by X-ray photoelectron spectroscopy, Raman spectroscopy, and its X-ray absorption fine structure. It is found that the solubility of substitutional Mn in a ZnO lattice is very low, which is less than 0.4%. Mn ions first dissolve into the substitutional sites in the ZnO lattice, thereby forming $Mn^{2+}O_4$ tetrahedral coordination when $x \leq 0.001$, then entering into the interstitial sites and forming $Mn^{3+}O_6$ octahedral coordination when $x \geq 0.005$. All the samples exhibit paramagnetic behaviors at room temperature, and antiferromagnetic coupling can be observed below 100 K.

Keywords: magnetic semiconductors, X-ray absorption fine structure, impurity distribution, exchange and superexchange interactions

PACS: 75.50.Pp, 78.70.Dm, 61.72.sh, 75.30.Et **DOI:** 10.1088/1674-1056/22/10/107501

1. Introduction

As is well known, doping is an effective method of controlling the properties of semiconductor nanocrystals.[1,2] The research results show that there are different distributions of dopants, such as in substitutional sites, in interstitial sites, and in the surface of nanocrystals.[3,4] Understanding the role of dopants, including the dopant concentration, the position, bonding, and spatial distribution of the dopants, is fundamental in explaining the optical, luminescent, magnetic, or other physical properties of nanocrystals. Mn-doped ZnO system, as a candidate diluted magnetic semiconductor (DMS) material with a higher Curie temperature (T_C) than room temperature, has received much attention due to the theoretical predictions given by Dietl *et al.*[5] However, various experimental results of Mn-doped ZnO such as ferromagnetism (FM),[6] paramagnetism (PM)[7] or antiferromagnetism (AFM)[8] have been obtained by different research groups. Kundaliya *et al.*[9] found that the ferromagnetism in ZnMnO originated from oxygen-vacancy-stabilized $Mn_{2-x}Zn_xO_{3-\delta}$. Garcıá *et al.*[10] attributed the ferromagnetic behavior to the interaction between Mn^{3+} and Mn^{4+}. Lawes *et al.*[11] found that the dominant interactions in Mn-doped ZnO systems were antiferromagnetic and attributed this behavior to contributions from both Mn ions with Mn nearest neighbors and from isolated spins. From the above research results, we can see that the magnetic properties are seriously affected by the coordination environment of Mn ions in a ZnO lattice. It is very important to reveal the coordination environment of Mn in order to clarify the origin of magnetism in a Mn-doped ZnO system.

However, it is difficult to characterize the coordination environment of a dopant, especially in a diluted content. X-ray absorption fine structure (XAFS) is very sensitive to the local environment of a selected atom.[12] For example, Smolentsev *et al.*[13] have observed that the majority of Mn atoms substitute Zn atoms and there is cubic symmetry around Mn atoms in the ZnO wurtzite lattice in $Zn_{1-x}Mn_xO$ ($x = 0.005$, 0.01) films. Zhang *et al.*[14] have found that the Mn-doped ZnO system presents substantial paramagnetic behavior and the strong AFM interaction arises from the fact that Mn ions fill Zn sites only, forming spin-antiparallel pairs and inducing a large structural distortion Mn confirmed by XAFS spectra. In the present work, we systematically synthesize $Zn_{1-x}Mn_xO$ ($x = 0$, 0.0005, 0.001, 0.005, 0.01, 0.02) nanocrystals and investigate the variation of the coordination environment of Mn ions in a ZnO lattice with Mn content with XAFS, Raman and UV-Vis spectra. We also investigate the magnetic properties and magnetic coupling states of $Zn_{1-x}Mn_xO$ nanocrystals.

*Project supported by the National Basic Research Program of China (Grant No. 013CB934001) and the National Natural Science Foundation of China (Grant No. 51272015).

†Corresponding author. E-mail: whao@buaa.edu.cn
‡Corresponding author. E-mail: hzxu@buaa.edu.cn

© 2013 Chinese Physical Society and IOP Publishing Ltd

2. Experimental details

$Zn_{1-x}Mn_xO$ ($x = 0$, 0.0005, 0.001, 0.005, 0.01, 0.02) nanocrystals were synthesized by using a wet chemical process, as described by Schwartz *et al.*[15] The precursor salts (zinc acetate and manganese acetate) were dissolved in dimethylsulfoxide (DMSO) according to the desired stoichiometry. The total metal ion concentration was 0.1 M. Tetramethylammonium hydroxide (TMAH) was dissolved in ethanol, keeping the concentration at 0.55 M. Then the ethanolic solution of TMAH was added dropwise to the metal salt solution under constant stirring at room temperature. After 48 hours, the nanocrystals were precipitated by adding ethylacetate and removed from the supernatant by centrifugation. Finally, the precipitates were dried at 353 K and annealed at 873 K in air for 3 hours in order to remove the precursor.

The X-ray diffraction (XRD) patterns were recorded by using a Rigaku Dmax/C X-ray diffractometer using Cu Kα radiation operated at 40 kV and 200 mA. The crystalline structure was characterized by a JEM-2100F transmission electron microscope (TEM) at an accelerating voltage of 200 kV. The valence of Mn was collected by an X-ray photo-electron spectroscope (XPS VG ESCALAB 250). Mn *k*-edge XAFS spectra were measured in fluorescence mode due to the lower concentration of Mn on Beamline 1W1B at the Shanghai Synchrotron Radiation Facility. Raman spectra were detected by an HR800 LabRam Infinity spectrometer excited by a continuous Ar^+ laser with a wavelength of 514 nm. Magnetic measurements were carried out by using a Lake Shore M-7401 Vibrating Sample Magnetometer (VSM). The *M*–*T* curve was measured using a physical properties measurement system (PPMS; Quantum Design) equipped with a vibrating sample magnetometer over a temperature range from 5 K to 350 K.

3. Results and discussion

Figure 1(a) shows the XRD patterns of $Zn_{1-x}Mn_xO$ nanocrystals. All the diffraction peaks can be attributed to pure ZnO with a wurtzite structure. There is no detectable second phase in all samples. Figures 1(b)–1(d) show the dependences of lattice constant (a and c), cell volume (V) on the value of x in $Zn_{1-x}Mn_xO$ nanocrystals. The values of a, c, and V are almost unchanged when $x \leq 0.001$, then the values increase with the value of x increasing. This variation indicates that the lattice of ZnO begins to expand with the Mn content increasing when $x \geq 0.005$. According to Scherrer's formula, the grain sizes of the nanocrystals are about 30 nm ($x \leq 0.001$) and 20 nm ($x \geq 0.005$), respectively. As shown in Fig. 1(e), the grain sizes of $Zn_{1-x}Mn_xO$ nanocrystals are smaller than those of pure ZnO nanocrystals. It means that the dopants inhibit the growth of ZnO nanocrystals, which indicates that the dopants may distribute in the surface of ZnO particles as found by Norberg *et al.*[16] Figure 2(a) shows the energy dispersive spectrum (EDS) of $Zn_{0.98}Mn_{0.02}O$ nanocrystals. It reveals that the content of Mn is about 1.9%, which is close to the nominal concentration. As shown in Fig. 2(b), the grain size is about 20 nm which is in good agreement with the XRD result. Figures 2(c) and 2(d) show the high-resolution TEM (HRTEM) images of the nanocrystals. The spacings between adjacent lattice planes are about 0.258 nm and 0.242 nm, which equal the distance between two (002) and (101) planes in ZnO, respectively. It reveals that the $Zn_{1-x}Mn_xO$ nanocrystals are in the forms of the wurtzite structure of ZnO.

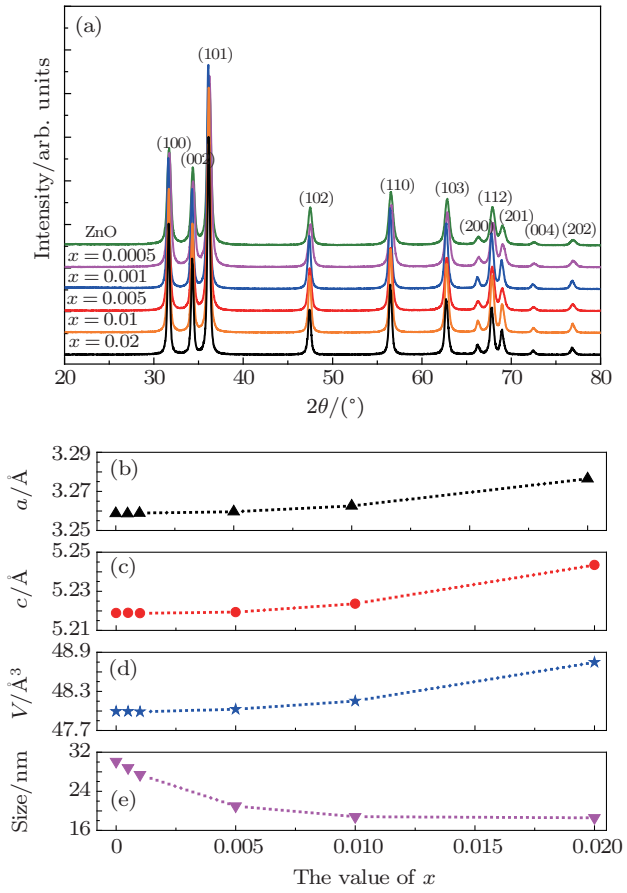


Fig. 1. (color online) XRD patterns of $Zn_{1-x}Mn_xO$ nanocrystals (a), variations of lattice constants (b) and (c), cell volume (V) (d), and grain sizes of $Zn_{1-x}Mn_xO$ nanocrystals (e) with the value of x.

Figure 3 shows the XPS spectrum of a $Zn_{0.98}Mn_{0.02}O$ nanocrystal. The binding energy is calibrated by taking a carbon C 1s peak (284.6 eV) as a reference. The Mn 2p peak is observed besides the C 1s, O 1s, Zn 2p, which indicates that no impurity elements are observed in our sample. The inset shows the Mn 2p XPS fine spectrum of our sample. The intensity of Mn 2p 1/2 is unobvious due to the contributions of Zn $L_2M_{23}M_{23}$ and $L_3M_{23}M_{23}$ Auger spectra.[17] The binding energy of the Mn 2p 3/2 peak is about 641.6 eV, which indicates that the valence of Mn is +3.[18] Therefore, there are no second phases and the main valence of Mn is about +3 in the sample with a high Mn content.

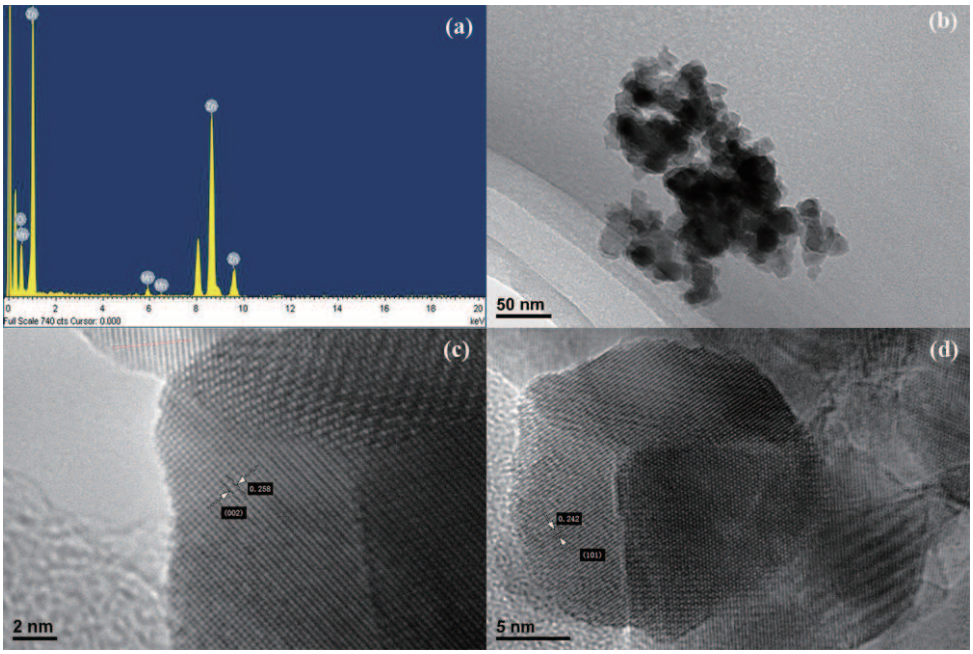


Fig. 2. (color online) Energy dispersive spectrum (a), TEM image (b), the high-resolution TEM images (c) and (d) of $Zn_{0.98}Mn_{0.02}O$ nanocrystals.

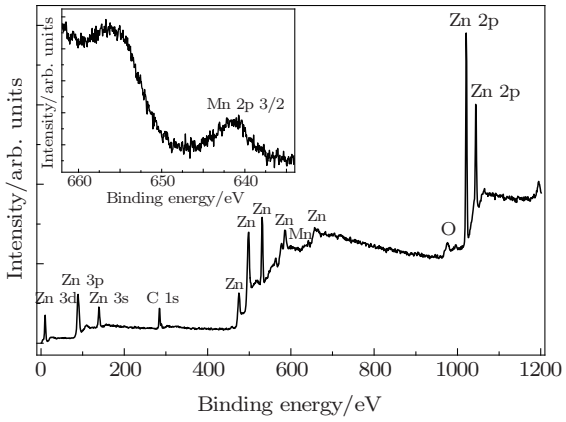


Fig. 3. XPS spectrum of $Zn_{0.98}Mn_{0.02}O$ nanocrystal, with the inset showing the Mn 2p XPS spectrum.

In order to further investigate the coordination environment of Mn in $Zn_{1-x}Mn_xO$ nanocrystals, especially at low concentrations of Mn, the normalized Mn *k*-edge XANES spectra of $Zn_{1-x}Mn_xO$, the reference samples MnO, and Mn_2O_3 are shown in Fig. 4(a). For comparison, the Zn *k*-edge XANES spectrum of ZnO is shifted to the position of the Mn *k*-edge spectrum. The Mn *k*-edge energy is used to characterize the average Mn oxidation state. When $x \leq 0.001$, the position of the white line peak of our sample is similar to that of MnO, which reveals that the Mn oxidation state is +2. When $x \geq 0.005$, the main edge energy shifts toward high energy, which indicates the average oxidation state increases with the value of x increasing. When x is equal to 0.01 or 0.02, the position of the white line peak is similar to that of Mn_2O_3, indicating that the valence of Mn is mainly +3. In addition, the similarity of features at the post-edge region between Mn *k*-edge and Zn *k*-edge in ZnO reveals the chemical environment of some Mn is the same as that of Zn in ZnO in the samples with low Mn content ($x \leq 0.001$). It means that part of Mn^{2+} ions substitute for Zn^{2+} ions in ZnO. While in the samples with high Mn content ($x \geq 0.005$), there is an obvious difference between Mn *k*-edge of $Zn_{1-x}Mn_xO$ and Zn *k*-edge of ZnO in the post-edge region. The difference shows that the chemical environment of Mn in the ZnMnO is different from that of Zn in ZnO, which indicates that the Mn^{3+} ions do not substitute for Zn ions in ZnMnO sample.

Figure 4(b) shows the Mn *k*-edge Fourier transform of $k^3\chi(k)$ functions of EXAFS spectra. For comparison, the Mn *k*-edges of MnO, Mn_2O_3, and MnOOH, as well as the Zn *k*-edge of pure ZnO are also illustrated. Here, P_1 (1.41 Å) and P_3 (2.41 Å) are attributed to the first Mn–O and the second Mn–Mn coordination shell of MnO_6 in MnOOH, respectively. P_2 (1.55 Å) and P_4 (2.93 Å) represent the first Zn–O and the second Zn–Zn shell in ZnO. Substituting Mn for Zn, the coordination of Mn in Mn-doped ZnO will be an MnO_4 tetrahedron. As is well known, there are two main positions of Mn in ZnO lattices after doping, one is MnO_6 octahedron at the interstitial site and the other is MnO_4 tetrahedron at the substitutional site (as shown in Fig. 5). As a result, P_1 and P_3 represent the MnO_6 octahedral coordination (interstitial Mn), while P_2 and P_4 represent the MnO_4 tetrahedral coordination (substitutional Mn) in ZnO lattice. In $Zn_{1-x}Mn_xO$ ($x = 0.001$) nanocrystals, the two peaks at 1.55 Å and 2.93 Å indicate that Mn ions are mainly at the substitutional site. In $Zn_{1-x}Mn_xO$ ($x = 0.005$) nanocrystal, there are three peaks denoted as *A*, *B*, and *C*. Peak *A* corresponds to the Mn–O coordination, which is located between peaks P_1 and P_2. The other two peaks *B* and *C* are located at the positions of P_3 and P_4, which repre-

sent the interstitial Mn and the substitutional Mn, respectively. The position of peak A situated between P_1 and P_2, as well as the coexisting of peaks B and C, indicates that there are two different coordination environments of Mn in $Zn_{1-x}Mn_xO$ ($x = 0.005$) nanocrystals. As shown in the inset of Fig. 4(b), the calculated areas of peaks B and C according to Gauss fitting indicate that the ratio of substitutional to interstitial Mn is about 4:1, which means the maximum content of substitutional Mn is about 0.4%. When $x \geq 0.01$, two main peaks at about 1.41 Å and 2.41 Å indicate that Mn mainly enters into interstitial site in the ZnO lattice.

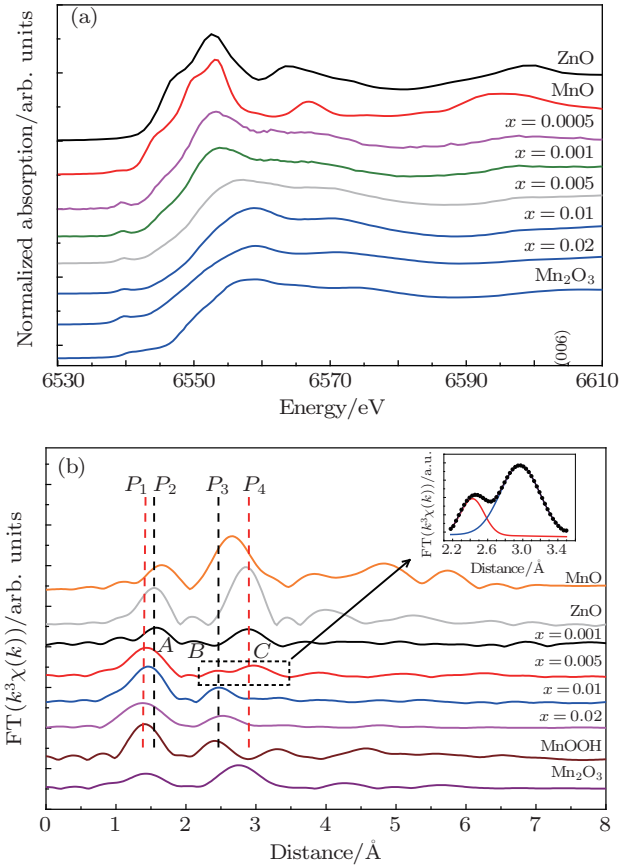


Fig. 4. (color online) (a) Normalized Mn k-edge XANES spectra of $Zn_{1-x}Mn_xO$ nanocrystals and the reference samples MnO, and Mn_2O_3. For comparison, the Zn k-edge XANES spectrum of reference ZnO is shifted to the position of the Mn k-edge XANES spectrum of MnO. (b) The Mn k-edge Fourier transform of $k^3\chi(k)$ functions of EXAFS spectra without phase correction for $Zn_{1-x}Mn_xO$ nanocrystals and reference samples MnO, Mn_2O_3, MnOOH, and ZnO. The inset shows the Gauss fitting of peaks B and C.

Figure 6 shows the UV-Vis absorption spectra of $Zn_{1-x}Mn_xO$ nanocrystals. The absorption at about 450 nm is due to the $^6A_1(S) \rightarrow {}^4T_1(G)$ transition of Mn^{2+} ligand-field in tetrahedral coordination.[19,20] The low intensity of this absorption indicates the concentrations of substitutional Mn ions are quite low in all samples, which is the same as the results of XAFS spectra. There is a broad absorption in a region of 600 nm–800 nm, which can be assigned to the charge–transfer transition between donor and/or acceptor levels as proposed in ZnMnS and ZnMnSe.[21] These donor and/or acceptor levels could be attributed to some defects in ZnO. The increasing intensity of this absorption means that the total defect density increases with Mn content increasing.

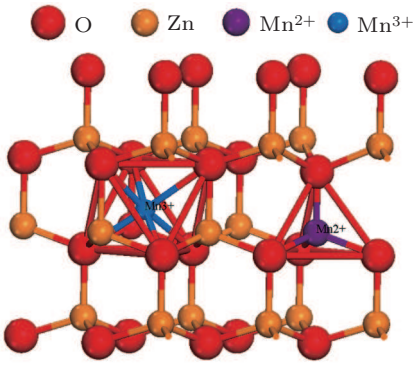


Fig. 5. (color online) Schematic diagram of the interstitial site and the substitution site Mn in a ZnO lattice after doping.

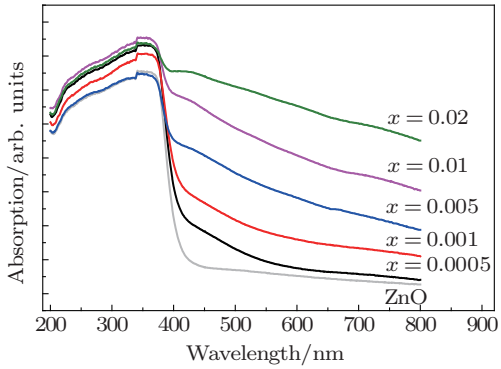


Fig. 6. (color online) UV absorption spectra of $Zn_{1-x}Mn_xO$ nanocrystals.

Figure 7 shows the Raman spectra of $Zn_{1-x}Mn_xO$ nanocrystals and pure ZnO. The four modes at about 332.3, 384.4, 438.6, and 579.9 cm^{-1} are assigned to 2-E_2(M), A_1^{TO}, E_2^{high}, and A_1^{LO} modes of pure ZnO, respectively.[22] The two additional modes at about 526.9 cm^{-1} and 665.1 cm^{-1} are denoted as AM_1 and AM_2, respectively. AM_1 is the mode induced by Mn^{2+} dissolving into the ZnO lattice as proved by Samanta.[23] The origin of AM_2 is still controversial. Samanta *et al.*[23] and Cong *et al.*[24] attributed it to the second phases $ZnMn_2O_4$ and $ZnMnO_3$, respectively. But there are no second phases in our samples. We have also noticed that this mode appears in the Raman spectra of Mn_2O_3[25] and MnOOH.[26] Among these four compounds, the coordination environments of Mn are in the form of a MnO_6 octahedron. As a result, we attribute AM_2 to the mode of MnO_6 octahedral coordination. As shown in Fig. 7, the increasing intensity of AM_2 indicates that the concentration of the MnO_6 octahedron increases with the value of x increasing, which is consistent with the results of the XAFS spectra. As a result, Mn ions are first to dissolve into

the substitutional sites in ZnO to form $Mn^{2+}O_4$ tetrahedral coordination and the solubility of substitutional Mn is very low (0.4% in nominal concentration). Then Mn ions enter into the interstitial sites to form $Mn^{3+}O_6$ octahedral coordination, the interstitial Mn increasing with Mn content increasing.

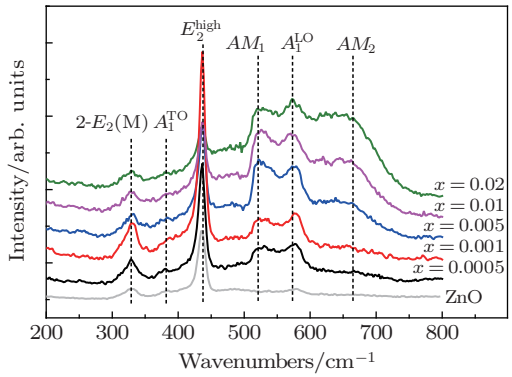


Fig. 7. (color online) Raman spectra of $Zn_{1-x}Mn_xO$ nanocrystals.

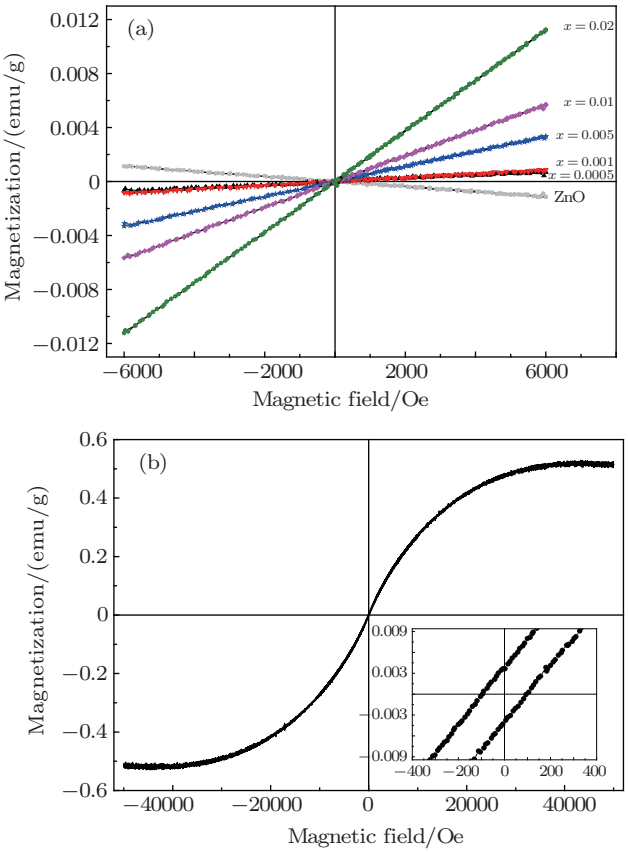


Fig. 8. (color online) M–H curves of $Zn_{1-x}Mn_xO$ nanocrystals at room temperature (a) and M–H curve of $Zn_{0.98}Mn_{0.02}O$ nanocrystals at 5 K (b). The inset shows the magnified low-field region. The unit 1 Oe = 79.5775 A·m^{-1}.

Figure 8(a) shows the room-temperature M–H curves of $Zn_{1-x}Mn_xO$ nanocrystals, together with pure ZnO nanocrystals synthesized in the same way. As shown in the figure, pure ZnO is diamagnetic, while the $Zn_{1-x}Mn_xO$ nanocrystals are paramagnetic and the magnetic moment increases with the value of $x$increasing. Figure 8(b) shows the M–H curve of $Zn_{0.98}Mn_{0.02}O$ nanocrystal at 5 K. The nanocrystal exhibits ferromagnetic behavior, as shown in the magnified low-field region. In order to further investigate the magnetic property, the curves of magnetization and the inverse magnetic susceptibility versus temperature (M–T and $1/\chi$–T) of $Zn_{0.98}Mn_{0.02}O$ nanocrystal are shown in Fig. 9. There is a magnetic phase transition at about 100 K, which has been considered as an AFM–PM phase transition.[27] However, the feature is not the same as the typical AFM–PM phase transition schematic diagram, as shown in the inset (a) of Fig. 9. In typical AFM–PM transition the value of $1/\chi$ increases with temperature decreasing below the phase transition temperature (T_P). As shown in the inset (b) of Fig. 9, $1/\chi$–T curve and T axis intersect at T_C in typical FM–PM transition. However, the magnetic phase transition curves of our samples are different from typical AFM–PM and FM–PM transition curves, in which $1/\chi$ decreases with temperature decreasing below T_P, and the $1/\chi$–T curve and T axis intersect at the origin point. It is the same as the stack of ferromagnetic and antiferromagnetic schematic $1/\chi$–T curves (shown in the inset (c) of Fig. 9).

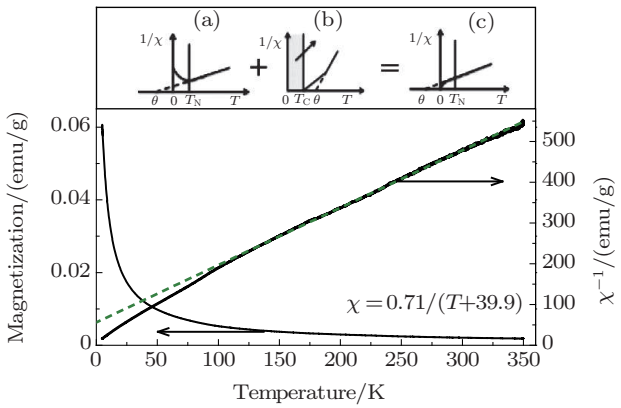


Fig. 9. M–T and $1/\chi$–T curves of $Zn_{0.98}Mn_{0.02}O$ in a temperature range from 5 K to 350 K in a magnetic field of 1000 Oe. The inset shows the schematic typical ferromagnetic (a) and antiferromagnetic (b) $1/\chi$–T curves, together with the stack of ferromagnetic and antiferromagnetic schematic $1/\chi$–T curves (c).

We suppose that it is the result of competing effect between the ferromagnetic and antiferromagnetic phase below T_P. The total moment below T_P increases due to the ferromagnetic moment as shown in Fig. 8(b). We suppose that FM maybe originates from the defects formed in ZnO (as proved by UV-Vis spectra), which is similar to the result of pure ZnO.[28] The data in high temperature region (above 100 K) is fitted to the Curie–Weiss law: $\chi = C/(T-\theta)$. From the fitted line (i.e., dot line) an extrapolated Curie temperature of $\theta = -39.9$ K is obtained, which indicates that the magnetic interactions between Mn ions are antiferromagnetic. As discussed above, most Mn ions in our nanocrystals enter into the

interstitial sites in the ZnO lattice and form $Mn^{3+}O_6$ groups with octahedral coordination. The neighboring Mn ions in the $Mn^{3+}O_6$ octahedron would be connected by O^{2-} between them and form an Mn^{3+}–O^{2-}–Mn^{3+} complex with the bond angle of 180°. According to the superexchange interaction,[29] one p electron of O would couple with the e_g orbital electron of Mn^{3+}. In addition, this electron in the p orbital of O must be antiparallel to the e_g orbital electron, which makes the two neighboring Mn^{3+} ions antiparallel. Thus, the system exhibits antiferromagnetic behavior. Our results also give a possible reason why the ferromagnetism cannot be observed in most Mn-doped ZnO DMS nanocrystals.

4. Conclusions

In this paper, we synthesize $Zn_{1-x}Mn_xO$ nanocrystals by using a wet chemical process. Our results indicate that Mn ions are first to enter into the substitutional site in ZnO lattice and form $Mn^{2+}O_4$ tetrahedral coordination at a low Mn content. With the increase of x, more Mn ions dissolve into the interstitial sites and form a $Mn^{3+}O_6$ octahedral coordination, which induces an antiferromagnetic coupling state between two Mn ions. We provide a promising perspective to explain why the ferromagnetism is hard to obtain in Mn-doped ZnO nanocrystals. Our results also indicate that it is important to investigate the environment of the dopants, which have significant effects on the magnetic properties and magnetic coupling state in doping semiconductor nanocrystals.

Acknowledgment

The authors would like to thank Beamline 1W1B at the Beijing Synchrotron Radiation Facility and Shanghai Synchrotron Radiation Facility for the measurements of Mn k-edge XAFS spectra.

References

[1] Erwin S C, Zu L, Haftel M I, Efros A L, Kennedy T A and Norris D J 2005 *Nature* **436** 91
[2] Alivisatos A P 1996 *Science* **271** 933
[3] Lommens P, Loncke F, Smet P F, Callens F, Poelman D, Vrielinck H and Hens Z 2007 *Chem. Mater.* **19** 5576
[4] Wang X, Song F, Chen Q, Wang T, Wang J, Liu P, Shen M, Wan J, Wang G and Xu J B 2010 *J. Am. Chem. Soc.* **132** 6492
[5] Dietl T, Ohno H, Matsukura F, Cibert J and Ferrand D 2000 *Science* **287** 1019
[6] Teng X Y, Yu W, Yang L H, Hao Q Y, Zhang L, Xu H J, Liu C C and Fu G S 2007 *Chin. Phys. Lett.* **24** 1073
[7] He Q B, Xu J Y, Li X H, Kamzin A and Kamzina L 2007 *Chin. Phys. Lett.* **24** 3499
[8] Fukumura T, Jin Z, Kawasaki M, Shono T, Hasegawa T, Koshihara S and Koinuma H 2001 *Appl. Phys. Lett.* **78** 958
[9] Kundaliya D C, Ogale S B, Lofland S E, Dhar S, Metting C J, Shinde S R, Ma Z, Varughese B, Ramanujachary K V, Salamanca-Riba L and Venkatesan T 2004 *Nat. Mater.* **3** 709
[10] García M A, Ruiz-González M L, Quesada A, Costa-Krämer J L, Fernández J F, Khatib S J, Wennberg A, Caballero A C, Martín-González M S, Villegas M, Briones F, González-Calbet J M and Hernando A 2005 *Phys. Rev. Lett.* **94** 217206
[11] Lawes G, Risbud A S, Ramirez A P and Seshadri R 2005 *Phys. Rev. B* **71** 045201
[12] Steven D C 2000 *Los Alamos Sci.* **26** 422
[13] Smolentsev N, Soldatov A V, Smolentsev G and Wei S Q 2009 *Solid State Commun.* **149** 1803
[14] Zhang L, Li J, Du Y, Wang J, Wei X, Zhou J, Cheng J, Chu W, Jiang Z, Huang Y, Yan C, Zhang S and Wu Z 2012 *New J. Phys.* **14** 013033
[15] Schwartz D A, Norberg N S, Nguyen Q P, Parker J M and Gamelin D R 2003 *J. Am. Chem. Soc.* **125** 13205
[16] Norberg N S, Kittilstved K R, Amonette J E, Kukkadapu R K, Schwartz D A and Gamelin D R 2004 *J. Am. Chem. Soc.* **126** 9387
[17] Riyadi S, Muafif, Nugroho A A, Rusydi A and Tjia M O 2007 *J. Phys.: Condens. Matter* **19** 476214
[18] Lu Y, Lin Y, Xie T, Shi S, Fan H and Wang D 2012 *Nanoscale* **4** 6393
[19] Beaulac R, Archer P I and Gamelin D R 2008 *J. Solid State Chem.* **181** 1582
[20] Rao C N R and Deepak F L 2005 *J. Mater. Chem.* **15** 573
[21] Mizokawa T and Fujimori A 1993 *Phys. Rev. B* **48** 14150
[22] Bundesmann C, Ashkenov N, Schubert M, Spemann D, Butz T, Kaidashev E M, Lorenz M and Grundmann M 2003 *Appl. Phys. Lett.* **83** 1974
[23] Samanta K, Dussan S, Katiyar R S and Bhattacharya P 2007 *Appl. Phys. Lett.* **90** 261903
[24] Cong C J, Liao L, Liu Q Y, Li J C and Zhang K L 2006 *Nanotechnology* **17** 1520
[25] Han Y F, Ramesh K, Chen L, Widjaja E, Chilukoti S and Chen F 2007 *J. Phys. Chem. C* **111** 2830
[26] Hu C C, Wu Y T and Chang K H 2008 *Chem. Mater.* **20** 2890
[27] Martínez B, Sandiumenge F, Balcells L, Arbiol J, Sibieude F and Monty C 2005 *Phys. Rev. B* **72** 165202
[28] Escudero R and Escamilla R 2011 *Solid State Commun.* **151** 97
[29] Nagamiya T, Yosida K and Kubo R 1955 *Adv. Phys.* **4** 1